POLAR SEA-ICE EXTENT DETECTION USING KU-BAND SCATTEROMETER DATA

Quinn P. Remund
Brigham Young University
459 CB, Provo, UT 84602
801-378-4884, 801-378-6586
remundq@ee.byu.edu

Abstract

Polar sea ice plays an important role in the global climate. Although spaceborne scatterometers such as NSCAT have low inherent spatial resolution, resolution enhancement techniques can be used to increase the utility of NSCAT data in monitoring sea ice extent in the polar regions. Dual polarization radar measurement parameters, A and B, are used to identify sea ice and ocean pixels in composite images where A is σ^o normalized to 40° and B is the incidence angle dependence of σ^o. The A polarization ratio (AV/AH), vertical polarization B values, and σ^o estimate error variance of the vertically polarized data contain useful information about the presence of sea ice. The A polarization ratio and BV are used as primary classification parameters to discriminate between sea ice and open ocean. Estimates of the sea ice extent are obtained using linear and quadratic (Mahalanobis distance) discriminant boundaries on the bivariate distribution. The distribution parameters needed for the quadratic estimate are taken from the linear estimate. The σ^o error variance is used to reduce errors in the linear and Mahalanobis ice/ocean classifications. Noise reduction is performed through binary image region growing and erosion/dilation techniques. The algorithm is applied to NSCAT data. The resulting edge closely matches the NSIDC SSM/I derived 30% ice concentration edge.

Introduction

Polar sea ice extent is a critical input to global climate and geophysical models. Polar ice acts as an insulating layer between the warmer ocean and cooler atmosphere and can radically change the albedo of the Earth's surface. It also plays a vital role in the planetary water exchange cycle. Polar sea ice extent may be used as a sensitive indicator of global climate change [1]. Hence, monitoring the extent of polar sea ice is of great interest to the remote sensing community. In this paper, an adaptive algorithm for detecting the polar sea ice edge from NSCAT data is developed and compared to SSM/I derived ice edges.

Historically, spaceborne scatterometers have been employed primarily in atmospheric and oceanic studies. Rapid repeat coverage makes these instruments valuable in these applications. The low spatial resolution of scatterometers is suitable for studying such large scale phenomena. Spaceborne scatterometers have also been used to study non-ocean surface parameters [2, 3]. However, for land and ice studies, the low resolution can limit the utility of this data.

The Scatterometer Image Reconstruction with Filter (SIRF) algorithm was developed to enhance scatterometer image resolution by combining data from multiple passes of the satellite [4]. It uses multiple σ^o values to increase the effective resolution of the data. Over a limited incidence angle range of [20°,55°], σ^o (in dB) is approximately a linear function of θ,

$$\sigma^o(\theta) = \mathcal{A} + \mathcal{B}(\theta - 40°)$$

where A and B are functions of surface characteristics, azimuth angle, and polarization. A is the σ^o value at 40° incidence and B describes the dependence of σ^o on θ. A and B provide valuable information about surface parameters. 40 degrees is chosen as a mid-swath value, but any interior swath angle can be used. The SIRF algorithm produces both A and B images from NSCAT σ^o measurements.

This paper describes the development and implementation of an adaptive sea ice edge detection algorithm. Section 2 describes the parameters to be used in a multivariate analysis of the data. Section 3 discusses multiparameter discrimination using different methods and determines the best combination of parameters. In section 4, residual noise reduction is considered in which digital image processing techniques are used to reduce misclassification errors. A detailed description of the algorithm is given in section 5. The algorithm is applied to NSCAT polar data and the results are given in section 6. The final section contains the conclusions drawn from the analysis.

Polar NSCAT Data

The NASA Scatterometer (NSCAT) launched in August of 1996 is a real aperture dual polarization Ku-band radar scatterometer designed to measure the normalized radar backscatter coefficient (σ^o) of the Earth's surface. Using the SIRF algorithm, dual polarization A and B images with an effective resolution of 8-10 km can be generated with 6 days of data. NSCAT V pol images can be produced with only 3 days of data since there are more V pol antenna beams than H pol beams. However, 6 days are used to ensure that the H pol data provides enough

coverage to create the reconstructed image. Since the V pol image has more measurements, the quality of the A and B estimates is superior to the H pol image. The dual polarization A and B values for each pixel provide four parameters that can be used to detect polar sea ice. In addition, σ^o error standard deviation is also useful. Each of these parameters contain different information about the surface that may be useful in the discriminant analysis. This section examines the statistical properties of these variables and their utility in the discrimination between polar sea ice and open ocean.

Polarization Ratio

The polarization ratio is defined as the ratio of σ_{vv} and σ_{hh} [5]. This can be extended to a polarization ratio of the incidence angle normalized σ^o values. For the purposes of this paper, the polarization ratio γ is defined as the ratio of the AV and AH values:

$$\gamma = AV/AH. \quad (1)$$

In log space, this is equivalent to taking the difference between the V and H components. Sample AV and AH images are shown in Figures 1a-b. The corresponding γ image is shown in Figure 1e. The polarization ratio is useful in determining the amount of volume versus surface scattering [5]. For smooth, conductive surfaces such as sea water, different reflection coefficients exist for vertically and horizontally polarized incident waves. In general, vertically polarized waves will reflect more than their horizontal counterparts. Thus, the polarization ratio will be positive (in dB). In volume scattering situations from dielectric surfaces with randomly oriented scatterers, such as ice with low water content, multiple reflections of the incident radiation tends to depolarize it. As a result, vertical and horizontal waves are scattered similarly and the polarization ratio is very close to unity. Because of the differences in scattering mechanisms, γ is useful in discriminating between different surfaces.

While the ocean will generally have high γ values and sea ice (with low water content) will generally have low values, in high wind conditions some ocean areas may exhibit low polarization ratios. The winds induce roughness on the ocean surface which depolarizes the scattering and drives γ down. To minimize the effects of this, the other parameters are used to assist in the classification.

Incidence Angle Dependence

B values represent the incidence angle dependence of σ^o. This parameter is useful for ice/ocean discrimination [5, 6]. Figures 1c-d give examples of BV and BH enhanced resolution images, respectively. Ice tends to be more isotropic [7] than open water and has less incidence angle dependence. Ocean σ^o is strongly dependent on incidence angle with the low incidence angles exhibiting higher σ^o.

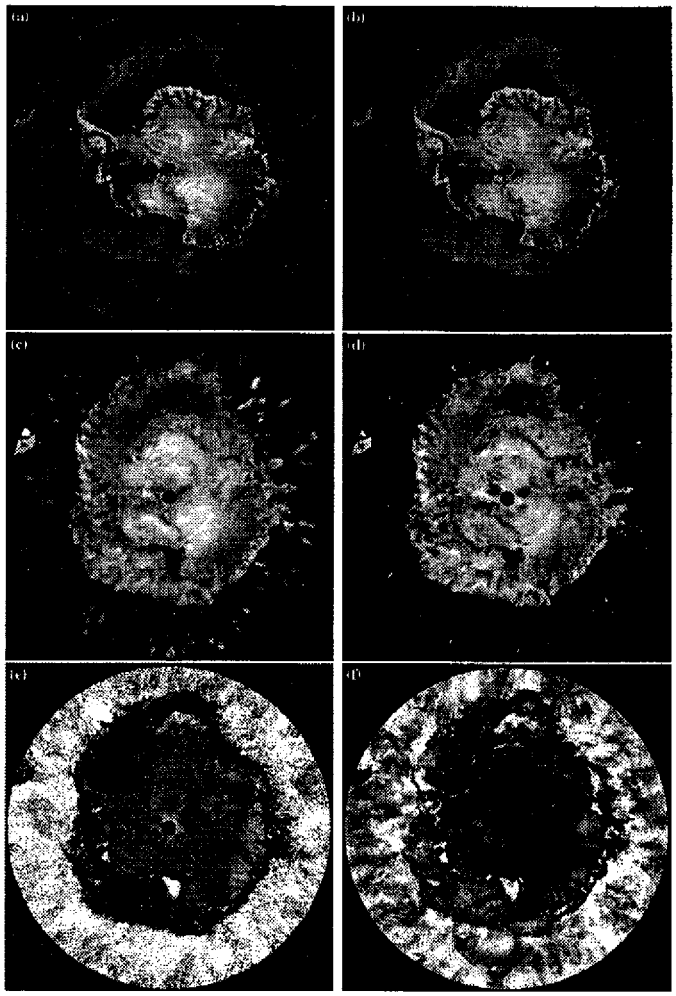

Figure 1: SIRF enhanced resolution NSCAT Antarctic images for the day range 1996 JD 337-342. The image panels contain (a) AV, (b) AH, (c) BV, (d) BH, (e) polarization ratio, and (f) σ^o error standard deviation. Each image demonstrates that it contains information about the presence of sea ice.

The study found a strong correlation between BV and BH. Noting that BV values are less noisy than BH due to the greater number of vertical polarization measurements, BV was chosen for the discriminant analysis in this study.

σ^o Estimate Error Standard Deviation

The standard deviation of the error in the σ^o estimates also contains information about polar surfaces. This metric, denoted κ, is a measure of the amount of surface response change over the ensemble of σ^o measurements and is described below.

Each NSCAT fan beam antenna illumination pattern is resolved in the along beam direction through Doppler filtering along isodoppler lines in the footprint [8]. The

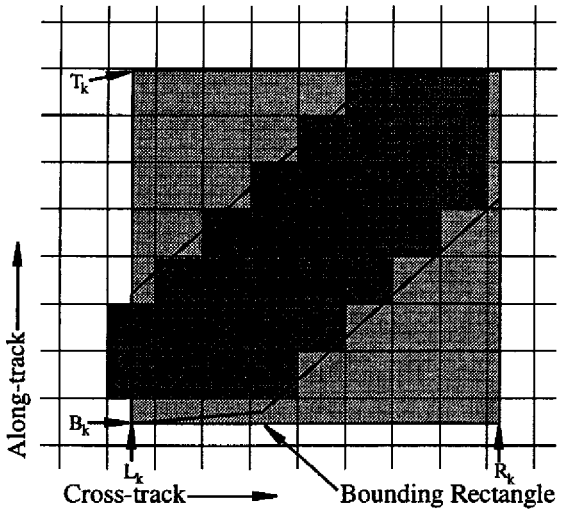

Figure 2: An integrated NSCAT σ^o cell overlaying the high resolution grid. Only the shaded square grid elements have nonzero $h(x,y)$. The bounding rectangle is also indicated.

beam is resolved into 25 cells at different incidence angles. The size of each cell depends upon its relative location in the beam with near nadir cells covering a smaller area on the surface. The cells have a hexagonal shape determined by the Doppler filtering, motion of the satellite, and azimuth beamwidth of the antenna [8].

Figure 2 shows an example NSCAT cell overlaid on a SIRF resolution grid. SIRF produces A and B estimates for each resolution element. The forward projection of the A and B values yields an estimate for σ^o given by

$$\widehat{\sigma}^o = \frac{1}{N} \sum_{i=L_k}^{R_k} \sum_{j=B_k}^{T_k} h_k(i,j)[A(i,j) + B(i,j)(\theta - 40^o)] \quad (2)$$

where N is the number of pixels in the cell, L_k, R_k, T_k, and B_k define a bounding rectangle for the k^{th} hexagonal σ^o measurement cell, $h_k(i,j)$ is the weighting function for the $(i,j)^{th}$ resolution element (for NSCAT a simplified weighting can be used),

$$h_k(i,j) = \begin{cases} 1 & \textit{Pixel in } k^{th} \textit{ cell} \\ 0 & \textit{otherwise} \end{cases} \quad (3)$$

$A(i,j)$ is the A estimate for the $(i,j)^{th}$ resolution element, and $B(i,j)$ is the B estimate for that pixel (see Fig. 2). For each NSCAT σ^o measurement, we compute the associated forward projection $\widehat{\sigma}^o$. The difference between the measured and forward projected σ^o, (σ^o-$\widehat{\sigma}^o$) for each pixel is computed. The parameter κ is defined as the standard deviation of the measurements in the ensemble of this random variable for each pixel:

$$\kappa = \sqrt{\sum_l (\sigma_l^o - \widehat{\sigma}_l^o)^2} \quad (4)$$

where the σ_l^o are the vertical polarization measurements touching the pixel. While this study used the SIRF A and B estimates to compute κ, estimates obtained from linear regression and simple binning may also be used although the resulting κ images would have lower spatial resolution.

Figure 1f illustrates an example κ image. Ideally, the standard deviation, κ, would be zero if SIRF perfectly reconstructed the measurements into the A and B images. However, temporal change of the surface, noise in the σ^o measurements, and azimuthal modulation of σ^o may cause κ to increase. The ocean response tends to be very dynamic in both time and azimuth due to varying wind induced surface roughness resulting in large κ values. Although higher κ values are expected in ocean regions than for sea ice, consistently calm ocean areas during the data collection period may produce low κ values. Sea ice response, on the other hand, is less time dependent, although ice melt/freeze events or ice motion may cause some variance. It was shown in [7] that azimuthal modulation in sea ice regions is generally less than 1 dB for C-band ERS-1 data. A duplicate study was performed for NSCAT data and showed that the modulation was less than 0.6 dB in the same study regions [9].

Multi-Parameter Discrimination

The three parameters, γ, BV, and κ each contain information about the surface response which can be used to differentiate between sea ice and open ocean pixels in the images. Several different combinations of these values are examined, along with different methods of discrimination to map the spatial extent of sea ice. Multi-variate linear discrimination and Mahalanobis distance are both considered.

The two-dimensional distribution of non-land pixels for any two parameters demonstrates the utility of each of these parameters for sea ice discrimination. An example is shown in Figure 3 for γ and BV. The corresponding contour plot is shown as well. Distributions are similar in form for pairs of parameters. The distribution contains two distinct modes that separately correspond with sea ice and ocean pixels. The goal is to separate the modes in the ice/ocean discrimination with minimal error. From this figure, it is clear that the combination of two parameters enhances the discrimination ability over using either parameter individually. Through the proper choice of a discriminant boundary, the modes can be separated to attain an ice extent estimate. Due to the seasonal variations in ice extent and scattering characteristics, the distribution is season dependent. Thus, the optimal mode-separating

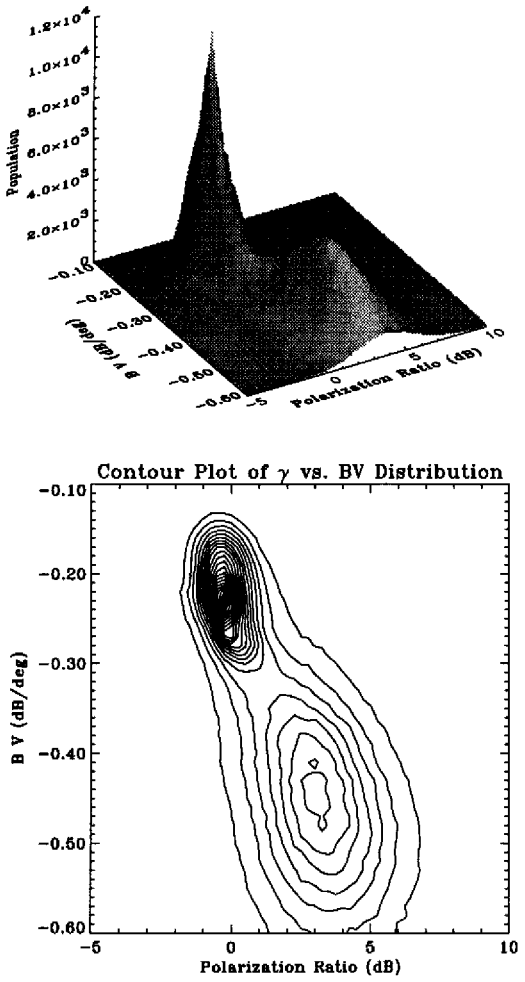

Figure 3: Two-dimensional distribution of polarization ratio values vs. BV values and its corresponding contour plot for NSCAT data from 1996 JD 337-342. The two modes represent ice and ocean pixels. Each mode clearly has different mean and variance values. The upper left mode is sea ice, the other represents ocean pixels.

boundary must adapt to the specific distribution for each 6 day imaging period.

Linear Discrimination

If the ice and ocean modes of the distribution are Gaussian, the optimum linear discriminant boundary passes through the saddle point of the density function and is perpendicular to the line passing through the peaks of the two modes. This line can be found in an automated fashion. First, the mode peaks are located by a 5x5 bin search of the probability density function. A 5x5 window of distribution bins is initially located in a region that is known to be in the ocean part of the distribution. The center of the 5x5 region is moved to the location of the bin with the maximum population value in the window. The center bin continues to move, ascending the ocean mode until the window is centered on the peak of the ocean mode. A 5x5 window is used to ensure that the algorithm does not get hung on any local maxima. A similar procedure is followed to locate the ice mode peak. The saddle point is then located along the line connecting the two peaks of the distribution at the bin with the minimum value along the line. The linear discriminant boundary is computed as a line passing through the saddle point and perpendicular to the peak to peak line. This can easily be extended to the three parameter case where the discriminant boundary is a plane passing through the three-dimensional space.

Once the linear discrimination boundary is computed, each pixel is classified as ice or ocean by comparing its associated parameter values with the decision boundary. Pixels on one side of the line are considered ice while the others are classified as ocean. Ice and ocean pixels in the resulting image are assigned values of one and zero, respectively. Figure 4 shows the γ vs. BV distribution contour plots of images from four different NSCAT time frames. The linear discriminant boundary is also plotted. Note that as the distribution characteristics change with season, the algorithm adaptively assigns an optimum decision boundary. The result of the linear discrimination is a binary image of ice and ocean locations.

Once an ice extent estimate image is produced, the means, variances, and covariances are computed for the ice pixels and the ocean pixels. These are used as statistical estimates for the Mahalanobis distance classification.

Mahalanobis Distance Discrimination

The Mahalanobis distance is a useful tool for separating the modes of a multimodal distribution where each mode is Gaussian with different variances. It accounts for the variance differences through the use of a quadratic rather than a linear boundary. The mathematical definition of the squared Mahalanobis distance is given by

$$r^2 = (\vec{x} - \vec{\mu})^T \Sigma^{-1} (\vec{x} - \vec{\mu}) \qquad (5)$$

where $\vec{x}$ is the vector of parameters for the test pixel, $\vec{\mu}$ is the reference vector containing the mode means, and Σ is the covariance matrix. If Eq. (5) is applied with three detection variables the quadratic boundary becomes a three-dimensional ellipsoid.

For each pixel of interest, two Mahalanobis distances are computed: r_{ice} and r_{ocean}. If r_{ice} is less than r_{ocean}, the pixel is flagged as ice, otherwise the pixel is considered ocean. Figure 4 shows the distribution contours plotted with the Mahalanobis and the linear discriminant boundaries.

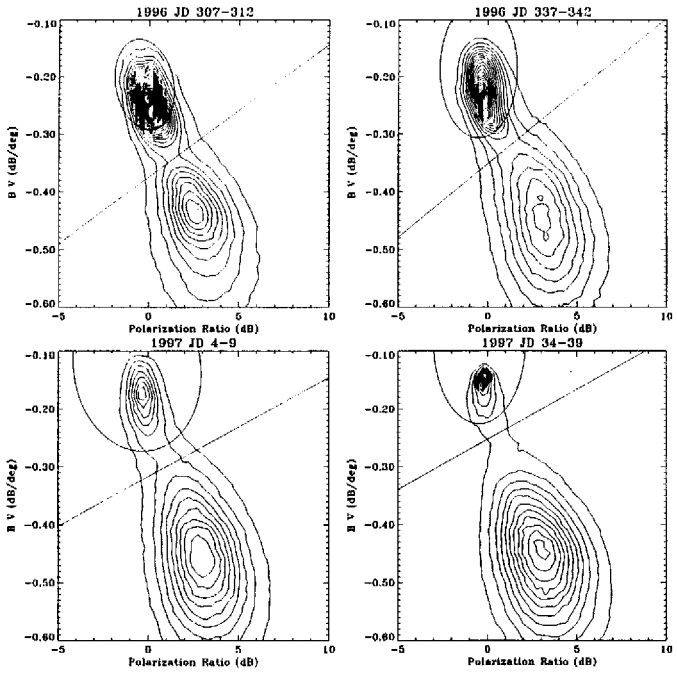

Figure 4: Contour plots of 4 polarization ratio vs. BV distributions. The Mahalanobis and the linear discriminant boundaries are also plotted. The decision boundaries are adapted to be optimum for each individual distribution.

Parameter Combinations

An exploratory study was performed to determine the effects of using different combinations of parameters in the linear and Mahalanobis discrimination processes. For all examples in this paper, SSM/I-derived ice concentration images were used for validation. This product is derived from passive multi-frequency, dual-polarization Special Sensor Microwave Imager (SSM/I) observations using the NSIDC algorithm [10]. The SSM/I images use the same polar stereographic projection used for the SIRF images but are produced at a much lower spatial resolution. For comparison to NSCAT results, the SSM/I ice concentration image for the same time period is thresholded at the desired concentration level and the edge is interpolated to the SIRF resolution.

First, the parameters, γ, BV, and κ, were used in the three-dimensional discrimination problem. The ice extent images were generated for several sample cases. In many cases, large underestimation errors were found in the edges. To determine the source of this error, all two parameter combinations were examined. Similar underestimation errors were found in all of the cases in which κ was one of the discrimination variables suggesting that κ is not useful as a primary discrimination parameter. The best edge estimates are obtained when the two parameter combination, γ and BV, is used. However, κ proved useful for correcting errors in the γ and BV discrimination.

σ^o Variance Correction

The linear discriminant (LD) and Mahalanobis distance (MD) binary ice extent images both provide visually good estimates of the ice edge when compared to the NSIDC edges. However, localized errors are observed in both. Local errors in the LD edge tend to overestimate the ice edge while MD usually underestimates the edge compared to the NSIDC algorithm. As described previously, consistently high winds during the data collection period may drive γ down resulting in a false ice detection when the LD method is applied. The same weather mechanism that causes this error also increases κ since high winds over the time frame of the data collection induce higher azimuthal modulation and temporal variance of σ^o. The overestimation error regions of the LD images have characteristically high κ values. The correlation between LD errors and high κ suggests that κ can be used as a secondary discrimination parameter to correct for errors in the LD and MD images.

The κ correction is applied to the set of all pixels for which the LD and MD images disagree. Thus, κ becomes the deciding factor when LD and MD yield different discrimination outputs. The set consists of all LD overestimation pixels and all MD underestimation pixels. An empirical analysis of the κ data over this set of pixels for several sample images showed that κ is generally above 3.3 for the LD error pixels. The correction is then applied by thresholding κ over the error set using the following discrimination rule:

$$pixel_{i,j}(\kappa_{i,j}) = \begin{cases} ice & \kappa_{i,j} < 3.3 \\ ocean & \kappa_{i,j} \geq 3.3 \end{cases} \quad (6)$$

where $\kappa_{i,j}$ is κ for the i,jth pixel in the set of pixels for which LD and MD disagree.

Residual Noise Reduction

The κ correction results in a binary image illustrating the location of sea ice and ocean regions. However, some residual high wind induced noise over the ocean can cause ocean pixels to be misclassified as ice for reasons previously addressed. This noise is manifested in the binary image as patches of ocean that have been classified as sea ice. Other physical mechanisms may also cause patches of ice to be misclassified as ocean. These anomalies often occur in isolated regions disconnected from the actual edge or on the edge. Each of these is handled separately in the noise removal step.

Region growing techniques are used to eliminate the isolated misclassification patches in the ocean and ice. The region growing algorithm starts with a small region known to be within the ice area (the land mass). It then expands

this region within the ice area of the binary ice mask image. The region continues to grow until it gets to the outer edge of the ice region and cannot expand further. This eliminates all the isolated patches of pixels misclassified as ice in the ocean. The region growing algorithm is then inverted to grow from the outer edge of the image inward until it reaches the binary threshold edge. This eliminates all the patches of pixels misclassified as ocean in the ice.

Once the region growing is complete, some residual noise exists on the edge itself as high spatial frequency edge characteristics and as small lobes attached by only a few pixels to the main body of ice. To remove these, image erosion and dilation techniques are used [11]. Two erosion iterations separate the smaller misclassified lobes from the main body. Region growing is then performed again to eliminate these separated lobes. To restore the edge (a low pass filtered version), two iterations of image dilation are performed. The result is a binary image mask that can be applied to the original A or B images.

Algorithm Description

The steps described above are combined to define an ice extent detection algorithm that adaptively handles the time variant parameter distribution. The algorithm can be summarized as follows:

1. Produce the enhanced resolution γ, BV, and κ images.
2. Generate γ vs. BV bivariate distribution of the images.
3. Perform linear discrimination to obtain a first estimate of the sea ice extent:
   (a) Linear discriminant boundary determination.
   (b) Pixel by pixel decision.
4. Compute the means, variances, and covariances of the ice and ocean regions for both parameters.
5. Perform the Mahalanobis distance discrimination.
6. Apply the κ correction by thresholding κ at 3.3 for all pixels for which the LD and MD estimates differ.
7. Reduce the residual noise.
   (a) Region growing removes isolated noise patches.
   (b) Erosion/dilation techniques low-pass filter the edge.

Results

The algorithm was implemented using SIRF resolution enhanced Antarctic images for the 4 time periods used in the distribution contour plots in Figure 4. Each time frame consists of 6 days of NSCAT data used to generate the necessary images. The images are each spaced by approximately one month to illustrate the changes in sea

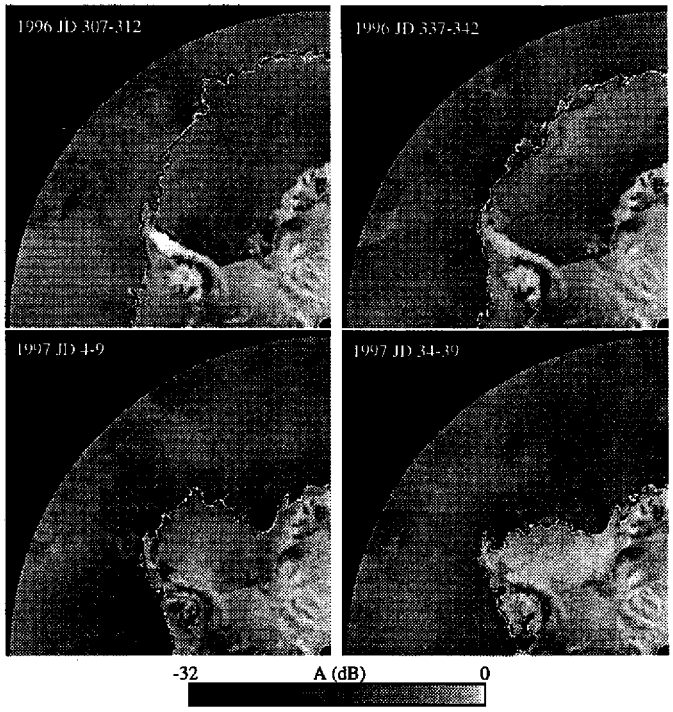

Figure 5: NSCAT SIRF resolution enhanced AV images of a portion of Antarctica. The NSCAT ice edge is plotted in white. The NSIDC SSM/I derived 30% ice concentration edge is plotted in black.

ice extent throughout the seasonal melt cycle. The resulting ice edges were compared with various NSIDC ice concentration images thresholded at different levels. The NSCAT ice edge corresponds most closely with a 30% ice concentration. This level is used as a reference edge in the comparisons that follow.

Figure 5 shows several sample SIRF AV images for a quadrant of Antarctica with the associated NSCAT and NSIDC 30% ice edge estimates. Subjectively, there is a high correlation between the edges. To provide a quantitative measure of correlation between the two ice maps, the disagreement percentage is used. This metric is defined as the ratio of the area of the pixels where the NSCAT and NSIDC methods disagree and the area of the pixels that are classified as ice by either method. For the images with time periods 1996 JD 307-312, 337-342, 1997 4-9, and 34-39, the disagreement percentages are 2.19%, 3.24%, 5.47%, and 3.56%, respectively. Figure 6 is a plot of this metric for the entire set of available coincident NSCAT and NSIDC data.

The seasonal sea ice extent in the polar regions can be monitored using the ice masked images from the algorithm. The sea ice extent for a particular image is computed by finding the area for each ice flagged pixel according to the polar stereographic projection. These areas are

summed to obtain the total extent. It should be noted that this is the total ice extent rather than the total ice area. Figure 7 shows the seasonal ice extent computed for the available NSCAT data set extending from 1996 JD 277-282 through 1997 JD 166-171. The melt cycle along with the beginning of the freeze cycle is evident. These results are similar in form to those of [12] in which the ice extent was computed using the Scanning Multichannel Microwave Radiometer (SMMR) from 1978-1987 although the maximum and minimum of the cycle are more extreme in 1996-1997.

The algorithm described is designed to detect the polar sea ice extent, and does not map open water regions within the ice pack. While the algorithm does locate polynyas and meltponds, these regions are filtered out in the region growing portion of the noise reduction stage. Slight modifications can be made to identify these regions and measure sea ice area rather than sea ice extent.

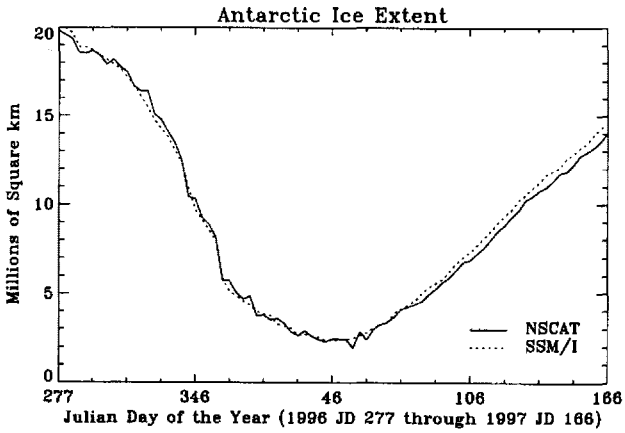

Figure 7: Seasonal Antarctic sea ice extent in square kilometers. The data set extends from 1996 JD 277-282 to 1997 JD 166-171.

Conclusion

NSCAT dual polarization Ku-band data in concert with the SIRF resolution enhancement algorithm can be used to effectively determine sea ice extent in the polar regions. The polarization ratio and the incidence angle dependence of σ^o are used as primary classification parameters since they appear to be the most sensitive to the presence of sea ice. The κ parameter on the other hand is useful for correcting errors in the linear and quadratic ice extent estimates due to its sensitivity to classification error inducing high winds in ocean regions. The algorithm requires no *a priori* information and adapts to the temporal variability of the underlying parameter distributions. When applied, the sea ice detection algorithm closely matches the NSIDC SSM/I-derived 30% ice concentration extent.

This study has shown that Ku-Band scatterometer data has utility in detecting polar sea ice. Although the NSCAT instrument was tragically lost in June 1997, the techniques developed in this paper may be applied to Seawinds, NASA's next generation scatterometer. Seawinds will also be a dual polarization Ku-Band instrument but will use a scanning pencil beam rather than fan beam antenna configuration.

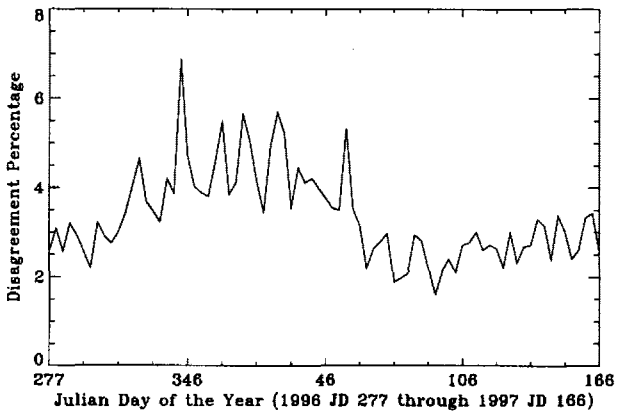

Figure 6: Plot of disagreement percentage metric computed by taking the ratio of surface area where the two methods disagree and the area for which either method classifies the surface as sea ice. The images each represent six days of data with three days of overlap between consecutive images. The Julian days given on the horizontal axis correspond to the first days of each imaging period.

References

[1] W.F. Budd, "Antarctic sea ice variations from satellite sensing in relation to climate," *IEEE Trans. on Geosci. and Rem. Sens.*, vol. 15, pp. 417–426, 1975.

[2] D. Long and M. Drinkwater, "Greenland Ice-Sheet Surface Properties Observed by the Seasat-A Scatterometer at Enhanced Resolution," *J. of Glaciology*, vol. 40, no. 135, pp. 213–230, 1994.

[3] A. R. Hosseinmostafa, V. I. Lytle, K. C. Jezek, S. P. Gogineni, S. F. Ackley, and R. K. Moore, "Comparison of Radar Backscatter from Antarctic and Arctic Sea Ice," *J. of Electromagnetic Waves and Applications*, vol. 9, no. 3, pp. 421–438, 1995.

[4] D. Long, P. Hardin, and P. Whiting, "Resolution Enhancement of Spaceborne Scatterometer Data," *IEEE Trans. on Geosci. and Rem. Sens.*, vol. 31, pp. 700–715, 1993.

[5] S.H. Yueh, R. Kwok, S. Lou, and W. Tsai, "Sea Ice Identification Using Dual-Polarized Ku-Band Scatterometer

Data," *IEEE Trans. on Geosci. and Rem. Sens.*, vol. 35, no. 3, pp. 560–569, May 1997.

[6] J.W. Rouse, "Arctic Ice Type Identification by Radar," *Proceedings of the IEEE*, vol. 57, no. 4, pp. 605-611, April 1969.

[7] D.S. Early and D.G. Long, "Azimuthal Modulation of C-Band Scatterometer σ^o Over Southern Ocean Sea Ice," *IEEE Trans. on Geosci. and Rem. Sens.*, vol. 35, no. 5, pp. 1201–1209, Sept. 1997.

[8] F.M. Naderi, M.H. Freilich, and D.G. Long, "Spaceborne Radar Measurement of Wind Velocity Over the Ocean–An Overview of the NSCAT Scatterometer System," *Proceedings of the IEEE*, vol. 79, no. 6, pp. 850–866, June 1991.

[9] Q.P. Remund, D.S. Early, and D.G. Long, "Azimuthal Modulation of Ku-Band Scatterometer σ^o Over the Antarctic," *BYU MERS Technical Report*, no. 97-02, July 1997.

[10] D.J. Cavalieri, C.L. Parkinson, P. Gloersen, and H.J. Zwally, "Arctic and Antarctic sea ice concentrations from multichannel passive-microwave satellite data sets: October 1978 to September 1995, User's Guide," *NASA Technical Memorandum 104647.*

[11] J.C. Rush, *The Image Processing Handbook, 2nd Ed.*, CRC Press, Boca Raton, FL, 1995.

[12] P. Gloersen, W.J. Campbell, D.J. Cavalieri, J.C. Comiso, C.L. Parkinson, H.J. Zwally, "Arctic and Antarctic Sea Ice, 1978-1987: Satellite Passive-Microwave Observations and Analysis," *Scientific and Technical Information Program*, National Aeronautics and Space Administration, Washington, D.C., 1992.